Full length article

A novel approach to investigate delta phase precipitation in cold-rolled 718 alloys

Zi Kang Low [a], Thibaut Chaise [a, *], Didier Bardel [c], Sophie Cazottes [b], Philippe Chaudet [a], Michel Perez [b], Daniel Nelias [a]

[a] Univ Lyon, INSA-Lyon, CNRS UMR5259, LaMCoS, F-69621, France
[b] Univ Lyon, INSA-Lyon, MATEIS CNRS UMR5510, F-69621, France
[c] Framatome, 10 rue Juliette Récamier, 69456, Lyon Cedex 06, France

ARTICLE INFO

ABSTRACT

This paper proposes a numerical alternative to the lengthy experimental approaches typically employed to characterize delta phase precipitation in 718 alloys. A high-throughput experimental case study is first performed on cold-rolled alloy 718 of known composition and initial microstructure. Direct resistance heating is used to generate highly heterogeneous thermal fields, which enables investigation of a wide range of temperatures with relatively few experiments. Through a coupled finite element and Kampmann-Wagner numerical model, topographies of delta phase characteristics resulting from the complex heat treatments are generated. The predicted precipitation state shows good agreement with scanning electron microscopy observations of the heat-treated samples, demonstrating the validity of the proposed numerical approach.

© 2018 Acta Materialia Inc. Published by Elsevier Ltd. All rights reserved.

1. Introduction

Alloy 718 (commonly known as Inconel®[1] 718) is the world's most widely used nickel-base superalloy, having extensive applications in the aerospace, petrochemical, and energy industries [1]. Many of its remarkable properties result from the precipitation of various intermetallic phases from the γ matrix. While the metastable γ'' phase is well-known for its strengthening effect, the stable δ phase is of particular interest with regards to the processing and in-service characteristics of the 718 alloy [2]. While there is still ongoing investigation on the effect of δ precipitates on the creep behavior of the alloy [3–5], moderate precipitation of the δ phase is known to reduce the notch sensitivity [6] and inhibit undesired grain growth during subsequent hot working [7]. For these reasons, at the design stage, the accurate prediction of δ phase characteristics (such as mass fraction, spatial distribution and precipitate size) is essential.

Classic design methods rely on existing experimental data in the form of temperature-time-transformation (TTT) diagrams, phase fraction evolution curves, or microscopic investigations [8–12] to predict the δ phase characteristics. However, a variety of factors may influence the precipitation kinetics and thus reduce the validity of such data. For instance, cold rolling has been found to promote δ phase precipitation [13] and affect precipitate morphology [1]. The δ solvus temperature has also been shown to vary with niobium content [14]. Re-establishing experimentally the precipitation data to take into account all possible variations in initial state is cost- and time-prohibitive. Indeed, the commonly used static method [15] involves isothermal treatments at various temperatures for up to 100 h [8], followed by fine-scale microstructural characterization [10]. Recent developments in high-throughput experimental techniques (e.g. the use of highly heterogeneous thermal loads [16] or combinatorial samples [17]) aim to reduce the time needed to construct such material libraries. Notably, the use of Joule heating to attain high temperatures allows significantly shorter heating and holding times (in the order of seconds or minutes) compared to traditional furnace heating.

Table 1
Composition of the alloy used in the experimental case study.

Element	Ni	Cr	Fe	Nb	Mo	Ti	Al	Si	Co	Mn	Cu	P	C	Ta
wt%	53.27	18.67	18.29	5.07	3.00	0.95	0.58	0.05	0.03	0.03	0.03	0.01	0.01	0.01
at%	52.59	20.80	18.98	3.16	1.81	1.15	1.25	0.10	0.03	0.03	0.03	0.02	0.05	~ 0

There is also strong interest in developing computational tools as they are capable of predicting the effect of variations in initial state or composition. Liu et al. [13] used the Avrami formalism [18] to model the effect of cold rolling and holding temperature on the δ phase fraction evolution. However, their approach only gives a phenomenological description fitted to a single configuration. Compared to this approach, precipitation models based on physical mechanisms at play are preferred, as they can provide a complete description of the evolution of different parameters of interest. Among the theoretical frameworks used in the past, Kampmann-Wagner Numerical (KWN) models [19] have been used to accurately predict the evolution of precipitate size, density, volume fraction, *etc.* in a simple and versatile manner [20]. Stockinger et al. [21] successfully applied the diffusion-controlled growth theory to reproduce the δ phase dissolution kinetics in alloy 718. Wu et al. [22] and Radis et al. [23] simulated the precipitation of various intermetallic phases including δ in alloys 718 and 718Plus respectively with KWN models. However, these work only focused on precipitation in strain-free alloys and do not account for the effect of cold rolling.

This paper proposes a novel approach combining Finite Element (FE) and KWN modeling to predict δ phase characteristics in samples submitted to heterogeneous heat treatments. An innovative high-throughput experimental technique inspired by Campello et al. [16] is used to demonstrate the applicability of the approach, through a case study conducted on 30% cold-rolled alloy 718 samples. The current work focuses specifically on modeling the effect of cold rolling, initial grain size and composition on δ phase precipitation in alloy 718. The particular case of hot forging is not covered here as the phenomena of grain deformation, δ phase dissolution, and precipitate breakage are present during forging [24].

Section 2 of this paper describes the high-throughput experimental method, in which direct resistance heating was used in this study to apply highly heterogeneous temperature fields to 718 alloy sheets. Microstructural characterization was then performed via scanning electron microscopy (SEM) and image processing. Section 3 describes the coupled FE-KWN models used to predict the resulting δ phase characteristics, which adapted recent developments in KWN modeling (*e.g.* Refs. [25,26]) to account for heterogeneous nucleation and non-spherical precipitates. The experimental and numerical results for the case study are compared in Section 4 to illustrate the reliability of the proposed approach in obtaining fast, precise, and robust predictions of δ phase characteristics.

2. Experimental technique

In this section, the high-throughput experimental technique is presented via a case study of short-term δ precipitation on cold-rolled alloy 718.

2.1. Material and sample preparation

The composition of the alloy used in this study is given in Table 1. Cast ingots were hot and cold rolled progressively into thin sheets, before undergoing a continuous solution treatment above
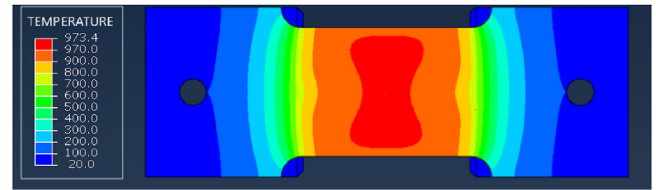

Fig. 1. Nodal temperature field (in $^\circ$C) at the end of holding for the 970° C/1800 s sample.

1050° C. Deleume et al. [27] observed for a similar process a grain size of ASTM 8—9 ($\simeq$ 20 μm) at this stage. The obtained metal sheets were further submitted to 30% cold rolling to achieve the final thickness of 0.27 mm.

Samples with lateral dimensions of 142 mm by 50 mm were cut parallel to the cold rolling axis. Ultrasonic cleaning was performed first with acetone, then with ethanol. Type K thermocouples were then welded to the central point and to various points on the longitudinal axis.

2.2. Heat treatments

Joule heat treatments were conducted on the samples using a Gleeble®[2] 3500 thermo-mechanical simulator. During each treatment, the sample was held at both ends by four copper grips cooled to 10° C. The apparatus was filled with argon to minimize oxidation, and a constant tensile force of 100 N was applied to the sample to prevent buckling upon thermal expansion. Samples were heated at a rate of 4.58 s^{-1} such that the temperature at the central point reaches the desired holding temperature (two different holding temperatures, 920° C and 970° C, were used in this study). They were then held for various holding times up to 60 min. Upon completion of the program, heat loss via conduction in the copper grips led to extremely fast cooling rates (of the order of -400° C during the first 5 s). FE modeling was used to obtain the full temperature fields, an example of which is shown in Fig. 1 (details on the model development and validation are given in Section 3.1).

The wide range of temperatures produced shows that the Joule heating method can indeed drastically reduce the number of heating cycles needed to cover the temperature range of interest for δ precipitation, which lies approximately between 700° C and 1000° C [3]).

2.3. Microstructural characterization

The δ phase was observed with SEM in Back-Scattered Electrons (BSE) mode at various points along the longitudinal axis, where the holding temperature gradient is the steepest. Metallographic specimens were machined from the heat-treated samples such that the longitudinal section is exposed. They were then hot-mounted in conductive resin, grounded and polished down to a 1 μm finish, and cleaned with acetone. A Zeiss Supra 55 V P microscope was used with an accelerating voltage of

---

[2] Gleeble is a registered trademark by Dynamic Systems Inc.
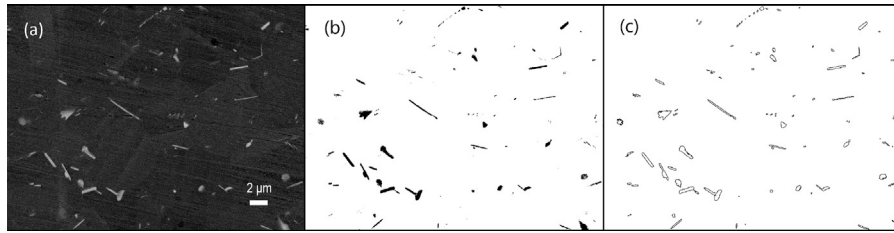
Fig. 2. Example of the application of the image processing method on the central point of the 970° C/1800 s sample. (a) Original SEM micrograph, (b) the corresponding binarized image, and (c) precipitates identified via particle analysis.

15 kV. Due to their chemical composition, in this mode, the δ precipitates appear white against a dark matrix. For each measurement point, around 30 images with a magnification of $3500\times$ and a pixel size of 30 nm, spanning a zone roughly 200 µm wide, were captured with a semi-automatic set-up.

The public-domain software ImageJ (version 1.51n under the Fiji distribution [28,29]) was used to threshold and binarize the obtained SEM micrographs. The precipitate volume fraction is taken to be equal to the area fraction [30] measured with the built-in particle analysis function. Particles of area less than $50 \times 50 \ nm^2$ were excluded; the contribution of δ precipitates below this size to the total area fraction has been verified to be negligible. Fig. 2 shows an example of the application of this process. With this method, more than 3000 particles are analyzed at each measurement point, with each particle comprised of 30 pixels on average.

3. Numerical models: development and calibration

The numerical approach proposed in this study predicts the δ phase characteristics in cold-rolled alloy 718 for any thermal process, irrespective of the heat treatment, geometry, or composition involved. For demonstration purposes, the approach is applied here to the experimental study conducted in Section 2. The strategy used to develop and validate the proposed approach, outlined in Fig. 3, is as follows:

1. Model the heat treatment with the FE method to predict the thermal history of the whole sample.
2. Validate the thermal history with temperature measurements taken during the heat treatments.
3. Develop and calibrate a KWN δ precipitation model.
4. Assuming one-way coupling between the temperature and microstructure, run the KWN model with the composition, grain size, cold rolling reduction ratio and thermal history at every node of the FE model.
5. Validate the precipitation state with the results of the SEM phase analysis.

3.1. Finite element modeling of the heat treatments

A FE model of the heterogeneous heat treatments was developed using the general-purpose finite element software Abaqus®/ Standard by SIMULIA®[3] (version 6.14–5 [31]), with the aim of reproducing the thermal history of the whole sample during the Gleeble heat treatments. Due to the presence of unknown parameters, an inverse optimization method was used similar to the what was done by Zhang et al. [32].

---

[3] Abaqus and SIMULIA are trademarks or registered trademarks of Dassault Systèmes or its subsidiaries in the United States and/or other countries.

3.1.1. Geometry and mesh

In addition to the heat-treated alloy 718 sample, the copper grips and thermocouples were also included in the FE model, as shown in Fig. 4(a). Linear elements with displacement, temperature, and electrical potential degrees of freedom were used to mesh the different parts. For the sample, a mesh sensitivity study led to the choice of Q3D4 tetrahedral elements of global size 2 mm, with a refinement by a factor of 10 in the central zone (Fig. 4(b)). The copper grips and thermocouples were meshed with Q3D8 brick elements of size 2 mm and 0.125 mm respectively.

3.1.2. Key boundary conditions

3.1.2.1. Contact.
As the thermocouples are welded onto the sample surface, a tie constraint is imposed between them. On the other hand, a rough, non-separating contact with interface conductances is applied between the grips and the sample. A relatively low thermal conductance value of $10 \text{W} \cdot \text{m}^{-1} \cdot \text{K}$ was identified via the method in 3.1.4, which can be explained by the contact surface roughness and prior oxidation of the grips. For the electrical conductance, an arbitrarily high value of $1 \times 10^{10} \text{W} \cdot \text{m}^{-1} \cdot \text{K}$ was used.

3.1.2.2. Temperature.
The inclined surfaces of the copper grips were fixed at 10° C to simulate the cooling by the jaws. The temperature at the tips of the thermocouples were fixed at room temperature (20° C).

3.1.2.3. Voltage.
The voltage profile was applied by varying the electric potentials on the inclined surfaces of the copper grips.

3.1.2.4. Losses.
Heat loss from the sample to the surroundings via radiation and convection is modeled. The sink temperature was set as 20° C.

3.1.3. Governing equations

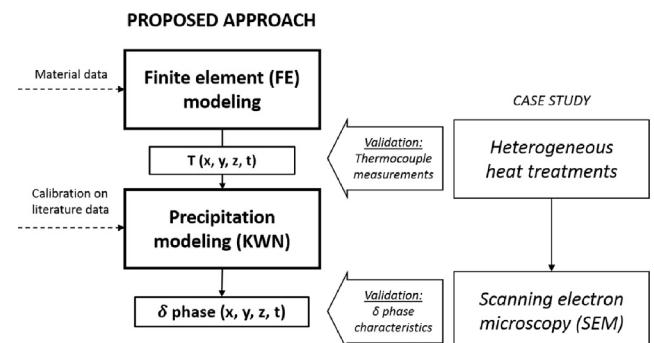The transient fully coupled thermal-electrical analysis

PROPOSED APPROACH

Fig. 3. Outline of the strategy used to develop and validate the proposed approach.

(a)

Copper grips
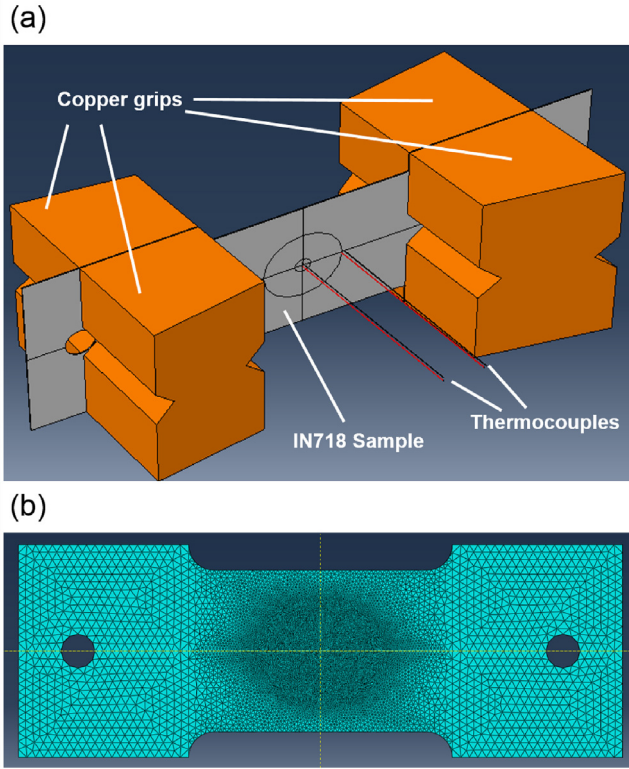
IN718 Sample

Thermocouples

(b)

Fig. 4. Geometry of the FE model (a), with the tetrahedral mesh used on the sample model (b).

procedure was used to solve for the thermal history at each node. As no phase change occurs during the heat treatments, the energy conservation equation is written as (1) for a material of density ρ, specific heat C_P, and thermal conductivity λ:

$$\rho C_P \frac{dT}{dt} - \nabla \cdot (\lambda \nabla T) = P_v^{elec} \qquad (1)$$

where T is the temperature in K, ∇ is the del operator, and P_v^{elec} is the volume heat source associated with Joule heating, defined as (2):

$$P_v^{elec} = (\nabla \varphi) \cdot \kappa \cdot (\nabla \varphi) \qquad (2)$$

where φ is the electric potential and κ is the electrical conductivity tensor.

At the sample surface, the radiative and convective heat losses to the environment are taken into account as per (3):

$$-\lambda \nabla T = \varepsilon \sigma_{SB} \left(T^4 - T_\infty^4 \right) + h_{conv}(T - T_\infty) \qquad (3)$$

where $\varepsilon = 0.5$ is the emissivity [33], $\sigma_{SB} = 5.67 \times 10^{-8} \, \text{W} \cdot \text{m}^{-2} \cdot \text{K}^{-4}$ is the Stefan-Boltzmann constant, T_∞ is the sink (ambient) temperature, and h_{conv} is the convective heat transfer coefficient, calculated following horizontal plate natural convection formulae [34].

Temperature-dependent material behavior was implemented for the alloy 718 sample based on literature data (see Table 2 for the sources used). On the other hand, reference values at 20° C were taken for the copper grips [35] and the thermocouple wires [36], as their temperatures remain mostly constant throughout the treatments. All materials in this study were assumed to be isotropic.

3.1.4. Calibration and validation of the FE model

The actual voltage applied during heating is unknown as the Gleeble represents its power output as an angle between 0° (minimum) and 90° (maximum). As such, the voltage profile and the thermal conductance at the grip-sample interfaces had to be calibrated to reproduce the thermocouple measurements along the longitudinal axis.

Fig. 5(a) shows a typical evolution of the Gleeble power output, which allows one to distinguish the heating, holding and cooling phases. The modeled voltage profile consists of a linear ramp during heating, constant voltage during holding, followed by a step down to zero. As the heating, holding and cooling times are known from the experiments, the voltage profile can be constructed from a single parameter: the holding voltage.

The Nelder-Mead algorithm [40] was used to solve the inverse problem by finding the holding voltage and interface thermal conductance that minimizes the RMS difference between the simulated and measured temperature gradients at the end of holding. Fig. 5(b) shows a good agreement between the measured thermal history at the central point and that predicted with the calibrated values. The discrepancy at the start of heating is of little consequence in the present study as the temperatures are below 700° C, and do not significantly affect the predicted δ phase precipitation kinetics.

Fig. 6 shows that the model predictions lie within 1% of the experimental temperature values in $^\circ$C. The uncertainty in the thermocouple measurements arises from the fluctuations in the readings and the precision of the thermocouples.

3.2. δ phase precipitation modeling

The main challenges in modeling δ phase precipitation are linked to the complexities in the nucleation process, several of which are elaborated here. The δ phase has been frequently observed in the form of spheroids, needles, or plates [41,42], precipitating either through transformation of the γ'' phase or directly from the γ matrix depending on the temperature [43]. Heterogeneous nucleation at grain boundaries [3], slip bands [44], and stacking faults in the γ'' phase [43] has been reported. Furthermore, Liu et al. [13] showed that cold rolling promotes not only the direct precipitation of the δ phase from the γ matrix, but also the γ'' to δ transformation at lower temperatures. Jouiad et al. [45] found evidence of dislocations acting as diffusion pipe-lines for Nb solutes, which supports the first observation by Liu et al. [13].

A KWN model was developed in this study such that for a given cold rolling reduction, composition and initial grain size, accurate predictions of δ phase characteristics can be obtained. PreciSo, a C++ implementation of the "Lagrange-like multi-class approach" described by Perez et al. [20], was used to compute the δ phase characteristics of interest. The model was calibrated for the effect of cold rolling with experimental data from Liu et al. [13], chosen for the wealth of information in their work. Further validation was performed with the classic TTT diagrams for strain-free alloy 718 [8—12], as well as in Section 4 with the results of the experimental

Table 2
Material data used as input for the FE model, with the temperature ranges on which the literature values were given.

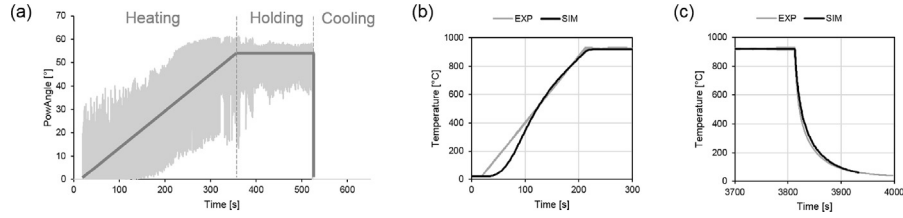| Properties	Temperatures	Ref.
Thermal conductivity	$21 - 1093^\circ$ C	[37]
Elec. conductivity	$21 - 1093^\circ$ C	[37]
Specific heat capacity	$21 - 1090^\circ$ C	[38]
Linear expansion	$20 - 871^\circ$ C	[39]
Density	$20 - 871^\circ$ C	[39]

Fig. 5. Calibration of the voltage profile. (a) Typical evolution of the Gleeble power output during heat treatments, with the dark line representing the modeled voltage profile. (b) Comparison between the measured (EXP) and predicted (SIM) thermal histories at the central point for the 920° C sample.

case study.

3.2.1. Description of the KWN model

Inspired by Wu et al. [22]'s approach, two populations of δ precipitates are considered in the present work so as to capture the aforementioned complexities. One population was modeled to nucleate exclusively on dislocations (noted δ_{disl}); while the other population was assumed to nucleate only on grain edges[4] (noted δ_{edge}). This latter hypothesis is particularly true in the high temperature domain ($\sim 900°$ C and above; see Section 4.1).

The following hypotheses were used in the current model:

- The chemical formula Ni_xNb_y with $x = 3$ and $y = 1$ was used for the δ phase. As nickel is present in abundance in the matrix, precipitation is supposed to be limited only by the diffusion of niobium.
- The only phases modeled were δ_{edge} and δ_{disl}; the association of a γ'' model to the present one will be detailed separately in a future work. The presence of other intermetallic phases was supposed to have no influence on the δ phase precipitation.
- The geometry of δ_{edge} was modeled as spherical, while δ_{disl} was modeled as needle-shaped (see Fig. 7). The aspect ratio is defined as $q = L/r_p$, where L is the length and r_p is the cross-sectional radius of the precipitate. In this model, the aspect ratio for both populations of δ were defined as $q_{edge} = 2$ and $q_{disl} = 7.6$, estimated based on past work [1,3,22] as well as the results of Section 4.1. Both parameters are supposed constant with respect to time and temperature as a first-order approximation.

3.2.2. Nucleation

As two δ phase populations are modeled, the subscript j is introduced in the following equations to denote either *edge* or *disl* depending on the nucleation site. When $q_j = 2$, the terms in $\{\cdot\}$ become unity, giving the classic equations for spherical precipitates.

Bardel et al. [25] expressed the critical radius r_{pj}^* (4) and the nucleation energy barrier ΔG_j^* (5) as follow:

$$r_{pj}^* = -\frac{2\Gamma_j}{\Delta g_j} \cdot \left\{ \frac{2q_j}{3q_j - 2} \right\} \tag{4}$$

$$\Delta G_j^* = f_j \cdot \frac{16}{3} \frac{\pi \Gamma_j^3}{\Delta g_j^2} \cdot \left\{ \frac{2q_j^3}{\left(3q_j - 2\right)^2} \right\} \tag{5}$$

where Δg_j is the chemical driving force for nucleation and Γ_j the matrix/precipitate interface energy. f_j is the heterogeneous

---

[4] Grain edges, as defined by Lorimer [46], are linear intergranular defects also known as triple junctions.
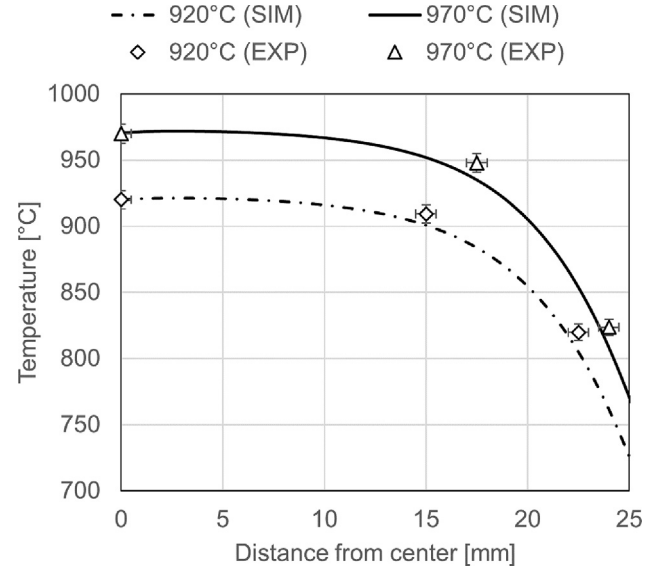

Fig. 6. Comparison of the temperature predictions of the FE model (SIM) against thermocouple measurements (EXP) along the longitudinal axes of the 920° C/1800 s and 970° C/1800 s samples; X = 0 mm corresponds to the central points.
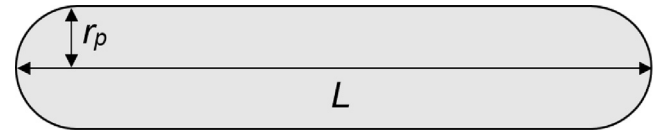

Fig. 7. Model of needle-shaped precipitates as cylinders of radius r_p and length $L - 2r_p$ capped at both ends by hemispheres of radius r_p [25].

nucleation coefficient, which represents a reduction of the nucleation barrier at grain edges [46] compared to dislocations:

$$f_j = \begin{cases} 1, & \text{if } j = disl \\ 0.2, & \text{if } j = edge \end{cases} \tag{6}$$

The classical nucleation rate J_{nj} is expressed as:

$$J_{nj} = N_{0j} Z_j \beta_j^* \exp\left(\frac{-\Delta G_j^*}{k_b T}\right) \cdot \left[1 - \exp\left(\frac{-t}{\tau_j}\right)\right] \tag{7}$$

where N_{0j} is the nucleation site density, β_j^* is the condensation rate, Z_j is the Zeldovich factor, and $\tau_j = 2/(\pi Z_j^2 \beta_j^*)$ is the precipitate incubation time. Z_j and β_j^* are calculated by (8) and (9) respectively:

$$Z_j = \frac{v_{at}^p(x+y)}{2\pi r_{pj}^{*2}}\sqrt{\frac{\Gamma_j}{k_BT}}\cdot\left\{\frac{\sqrt{8q}}{3q-2}\right\} \tag{8}$$

$$\beta_j^* = \frac{4\pi r_{pj}^{*2}}{a^4}X_{Nb}D_{Nb} \tag{9}$$

The temperature-dependence of the diffusion coefficient of niobium in the matrix D_{Nb} is assumed to follow an Arrhenius-type relation:

$$D_{Nb} = D_{Nb}^0\exp\left(-\frac{Q_{Nb}}{RT}\right) \tag{10}$$

To compute the real nucleation rate, one has to consider that both dislocations and grain edges may act as "short circuits" for solute diffusion. Perrard et al. [26] suggested two possible scenarios when a solute atom from the bulk arrives on a short circuit: the atom either forms a new precipitate, or diffuses rapidly along the dislocation to feed the growth of an existing one. A corrected nucleation rate is introduced:

$$\frac{dN_j}{dt} = J_{nj}\cdot\left[1-\exp\left(-\frac{\rho_j^2 J_{nj}}{2N_j^3(D_{Nb})_j}\right)\right] \tag{11}$$

where N_j is the instantaneous precipitate density, ρ_j is the dislocation or grain edge density, and $(D_{Nb})_j$ is the diffusion coefficient of niobium along the short circuits [26], taken here as $(D_{Nb})_j = 10^7 D_{Nb}$ for both $j = edge$ and $j = disl$.

Note that the current model does not directly account for the effect of misfit strain energy on precipitate nucleation. Instead, the Γ_j and f_j can be understood here as effective parameters that include the effect of strain energy, an approach that has given satisfactory results in previous works [20,25].

3.2.3. Growth

The growth of δ_{edge} follows the classic equation for spherical precipitate growth (12):

$$\frac{dr_{pedge}}{dt} = \frac{(D_{Nb})_{edge}}{r_{pedge}}\frac{X_{Nb}-X_{Nb}^i}{\alpha X_{Nb}^p - \left(X_{Nb}^i\right)_{disl}} \tag{12}$$

where X_{Nb}, X_{Nb}^i and X_{Nb}^p are the atomic fractions of niobium in the matrix, at the interface, and in the precipitates respectively; and $\alpha = v_{at}/v_{at}^p$ is the ratio between the matrix and precipitate atomic volumes.

On dislocations, δ_{disl} precipitates are modeled as needle-shaped and thus their growth follows (13), the adapted Zener-Hillert equation for needles [25]. More complex and complete treatments of the growth of non-spheroidal precipitates can been found in Refs. [47—49].

$$\frac{dL_{disl}}{dt} = 1.5\frac{(D_{Nb})_{disl}}{2r_{pdisl}}\frac{X_{Nb}-X_{Nb}^i}{\alpha X_{Nb}^p - \left(X_{Nb}^i\right)_{disl}} \tag{13}$$

The equilibrium atomic fractions at the interface are calculated taking into account the Gibbs-Thomson effect (14), with r_{0j} (15) being the capillary length:

$$X_{Ni}^{ix}\cdot X_{Nb}^{iy} = Ks\cdot\exp\left(\frac{r_{0j}}{r_{pj}}\right) \tag{14}$$

$$r_{0j} = \frac{2\Gamma_j v_{at}^p(x+y)}{k_bT}\cdot\left\{\frac{2q_j}{3q_j-2}\right\} \tag{15}$$

The solute concentrations are given by the solubility product Ks, which varies with temperature according to the quadratic Van't Hoff equation:

$$\log_{10}Ks = -\frac{A}{T}+B+\frac{C}{T^2} \tag{16}$$

where A, B and C are coefficients to be determined.

3.2.4. Calibration of the KWN model

While most of the input parameters required by the KWN model are well-documented, data on a few others are scarce or non-existent. The calibration of these parameters, based on the work of Liu et al. [13], is presented in this section. Models are proposed for their calculation where necessary, taking into account their dependence on the degree of cold rolling, composition and initial microstructure.

3.2.4.1. Solubility. The solubility product coefficients A, B and C in (16) can be obtained by performing a polynomial regression on literature data of Ks, shown in Fig. 8. As Ks theoretically only depends on the temperature and should not vary with the alloy used, aggregating data from multiple sources gives a value of Ks supposedly applicable to any composition of alloy 718. The effect of the composition on δ phase precipitation is thus implicitly taken into account.

3.2.4.2. Diffusion of niobium. Past work frequently refer to the diffusion coefficients of niobium measured by Ref. [51] or [52]; however these values are for the diffusion of niobium in pure nickel and are not necessarily valid in the presence of other alloying elements [53]. For niobium diffusion in alloy 718, Devaux et al. [54] found $Q = 272$ kJ·mol^{-1}, lower than 298kJ·mol^{-1} measured by Han et al. [55]; the difference was attributed to the difference in niobium composition (weight fraction 5.3% [54] against 4.94% [55]). In the present model, as the niobium weight fraction is 5.1%, Q was taken as 286kJ·mol^{-1}, with $D_{Nb}^0 = 8.8d - 5$m^2·s^{-1} following the example of Devaux et al. [54].

3.2.4.3. Nucleation site density. In the current model, the nucleation site density increases with cold rolling, due to grain
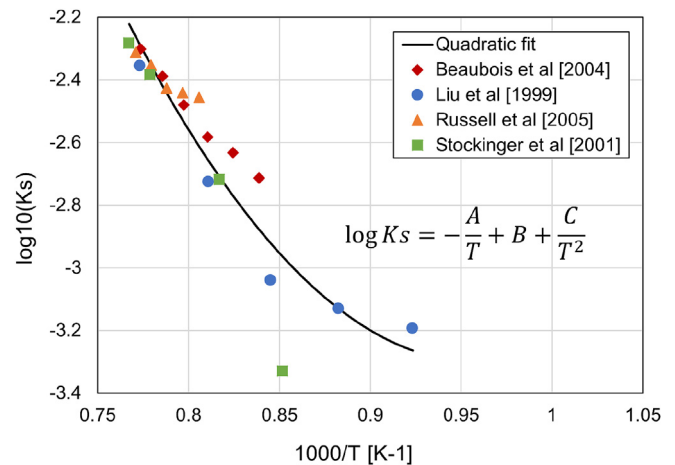

Fig. 8. Evaluation of the solubility product coefficients A, B and C via polynomial fitting to data from the literature [10,13,21,50]. Here $A = 5.66 \times 10^4$K, $B = 23.8$, and $C = 2.95 \times 10^7$K^2.

deformation and the creation of dislocations. Without quantitative data on this phenomenon, simplified models (demonstrated in Appendix A) were used to calculate the evolution of nucleation site density with cold rolling reduction ratio R. The pre-rolling grain size d and initial dislocation density ρ_{disl}^0 are also taken as input parameters.

The nucleation site density on the grain edges can be written as (17):

$$N_{0edge} = \frac{\rho_{edge}}{a} \quad \text{with} \rho_{edge} = \frac{1}{d^2}\left(3 + \frac{R^2}{1-R}\right) \tag{17}$$

On the other hand, the nucleation site density on dislocations is written as (18):

$$N_{0disl} = \frac{\rho_{disl}}{a} \quad \text{with} \rho_{disl} = \rho_{disl}^0 - \frac{2}{\sqrt{3}} \frac{\ln(1-R)}{bd} \tag{18}$$

Here the Burgers vector $b = a/\sqrt{2}$ [43] and the initial dislocation density ρ_{disl}^0 is taken as $1.5 \times 10^{13} \text{m}^{-2}$ according to data for alloy 690 [56].

3.2.4.4. Interface energy. Precise experimental determination of the precipitate-matrix interface energy Γ is notoriously challenging. By calibrating dissolution kinetics models through this parameter, previous works have found Γ values close to $0.095 \text{J}\cdot\text{m}^{-2}$ for the γ'' phase [54] and $0.1 \text{J}\cdot\text{m}^{-2}$ [21] for the δ phase. Radis et al. [23] calculated similar values for the δ phase in alloy 718Plus.

In the present study, precipitates nucleating on grain edges were modeled with different interface energies than those on dislocations, due to the different levels of crystalline defects as well as niobium segregation in these two sites. Γ_{edge} was assumed to be a constant $0.1 \text{J}\cdot\text{m}^{-2}$ as proposed by Stockinger et al. [21], whereas Γ_{disl} was chosen to be slightly higher, so as to favor the dissolution of the intra-granular precipitates (equations (14) and (15)) during long holding times, as observed by Ref. [3]. These values were assumed to be temperature-independent.

As cold rolling promotes niobium segregation on dislocations, it was supposed that Γ_{disl} decreases slightly with cold rolling. The value of Γ_{disl} was calibrated for cold rolling reduction ratios $R = \{0.25, 0.4, 0.5, 0.65\}$ based on experimental δ fraction data by Liu et al. [13]. A second-order polynomial function based the calibrated values is proposed in (19):

$$\Gamma_{disl} = aR^2 + bR + c \quad \text{with} \begin{cases} a = -5.5 \times 10^{-2} \\ b = -5.7 \times 10^{-4} \\ c = 0.118 \end{cases} \tag{19}$$

3.2.4.5. Aspect ratio. In the current model, the aspect ratio of the needle-shaped δ phase has been defined *a priori* according to SEM data: $q_{disl} = 7.6$. As Γ_{disl} was calibrated based on this value, if one were to vary q_{disl}, Γ_{disl} should be scaled according to (20) to preserve the surface energy-to-volume ratio and thus the nucleation kinetics. With this scaling, it was found that the model has very low sensitivity to q_{disl} values between 6 and 9.

$$\frac{\Gamma_{disl}\cdot q_{disl}}{(3q_{disl} - 2)^{2/3}} = constant \tag{20}$$

3.2.4.6. Results of calibration. The input data for $R = 0.25$ and $R = 0.65$, calculated according to the calibration method in this section, are listed in Table 3. The composition reported by Liu et al. [13] was

Table 3
Input parameters used to validate the δ precipitation model with experimental data by Liu et al. [13].

Param.	Values		Ref.
	δ_{edge}	δ_{disl}	
q_j	2	7.6	This study
N_{0j} [m^{-3}]	Eq. (17)	Eq. (18)	This study
Γ_j [J·m^{-2}]	0.1	Eq. (19)	[21], This study
a [m]	3.6077×10^{10}		[13]
ν_{at} [m^3]	1.1739×10^{29}		[13]
ν_{at}^p [m^3]	1.2312×10^{-29}		P [57]
D_{Nb}^0 [m$^2\cdot$s^{-1}]	$8.8d \times 10^{-5}$		[52,54]
Q_{Nb} [J·mol^{-1}]	2.86×10^5		[54,55]
A [K]	5.66×10^4		[10,13,21,50]
B	23.8		
C [K^2]	2.95×10^7		

used. Based on the solution treatment performed by the authors, the pre-rolling grain size was estimated at 90 μm [3].

The TTT diagrams for different cold rolling reduction ratios are traced in Fig. 9. The curves indicate the times at which the δ mass fraction reaches half of the equilibrium value[5] ($f_m = 0.5f_m^{max}$). The TTT diagrams each have two noses, as expected with two competing precipitate populations. The shape of the TTT at high temperatures is influenced mainly by δ_{edge} precipitation, while at low temperatures, the curve is influenced mainly by δ_{disl} precipitation.

Experimental data from Liu et al. [13] are also plotted on Fig. 9. At temperatures of 910° C and above, the curves show remarkable agreement with the experimental points, joining one another close to the solvus temperature. At lower temperatures (grey area on Fig. 9), the predicted curves fall to the left of the experimental points (*i.e.* the model predicts earlier precipitation). This is unsurprising as the current model does not yet take into account the presence of the γ'' phase, which competes with δ for the niobium solute at temperatures below its solvus ($\sim$900° C). The inclusion of the γ'' phase should improve the model on this point.

Fig. 10 shows the comparison between the measured [13] and predicted mass fraction evolution for the 25% cold-rolled sample at 910° C. The decomposition of the needle-shaped δ phase at long holding times was also predicted by the model.

3.2.5. Validation against literature data
An advantage of the calibrated model is its ability to reveal more information than what is usually given in the literature. For example, Liu et al. [13] did not provide any data on the precipitation kinetics in their alloy in the absence of cold rolling. Despite this fact, the strain-free precipitation kinetics of Liu et al. [13]'s alloy can still be predicted using the calibrated model.

Fig. 11 validates the generated TTT diagram for Liu et al. [13]'s alloy without cold rolling with experimental data from Refs. [8—12]. The curves correspond to the times at which trace amounts of δ phase were detected at each temperature. A close agreement is found with previously published TTT diagrams, notably with that by Oradei-Basile and Radavich [9], which can be due to the similarities in initial microstructure resulting from the preparation methods used.

Note that in this case, the model also predicts the appearance of δ_{edge} before δ_{disl} in accordance with Azadian et al. [3]'s observations.

---

[5] The equilibrium mass fraction is obtained by simulating extremely long holding times ($>10^8$ s) with the current model.
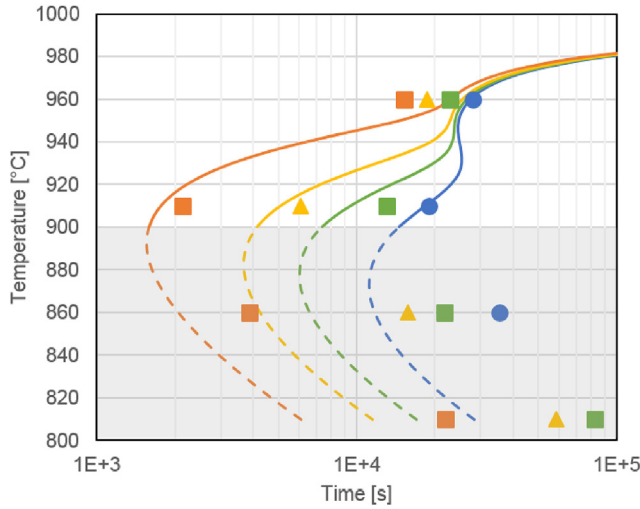
Fig. 9. Predicted (SIM) time-temperature-transformation (TTT) curves for different cold rolling reduction values, compared to experimental results (EXP) by Liu et al. [13]. Each curve marks the time at which the mass fraction $f_m = 0.5 f_m^{max}$. Shaded grey zone on the lower part of the graph show the precipitation domain of γ".
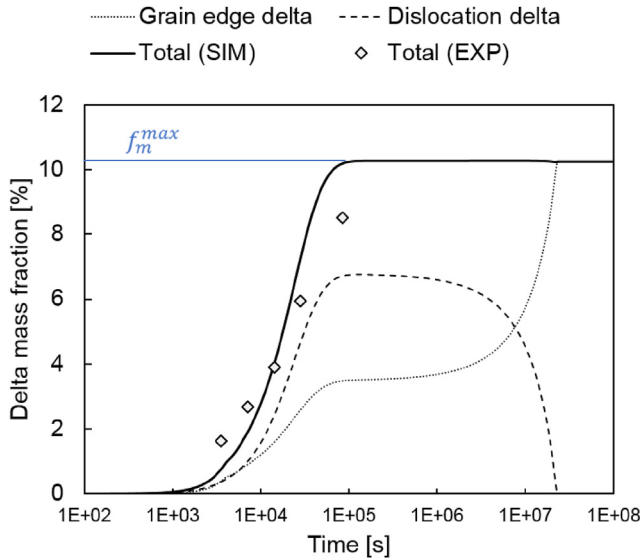

Fig. 10. Delta phase evolution in 25% cold-rolled alloy 718 at 910° C, showing the decomposition of the dislocation precipitates at long holding times.
Note that generally speaking, time-evolution curves predicted with a KWN model tend to have a steeper slope than the experimental measurements. This is because for a given precipitate population, the KWN model assumes that the nucleation barrier has the same value at all nucleation sites, while in real systems a variation exists between sites. Experimentally, nucleation first occurs rapidly at sites of low nucleation barriers, then slows down with time as the remaining sites become less favorable for nucleation. Moreover, a more precise modeling of the diffusion field in heterogeneous precipitation may also affect the precipitate growth rate, as shown by Kozeschnik et al. [58]. While these features are unaccounted for in the current model, they are compensated for by calibrating the model according to the times at which $f_m = 0.5 f_m^{max}$.

3.3. Coupling of the FE model to the precipitation model

With the KWN model calibrated and validated, the input data was updated with material data from the case study in Section 2:

- The alloy composition was updated with the data in Table 1.
- As the niobium content of the alloy used in the case study is very similar to that of Liu et al. [13]'s alloy (5.07% vs. 5.1%), it was supposed that the diffusion activation energy Q_{Nb} is unchanged.
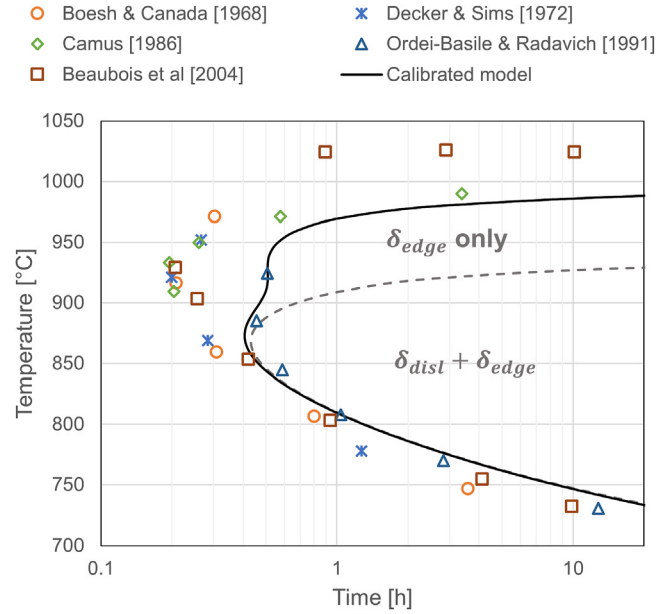

Fig. 11. Predicted TTT curve for the alloy used in the calibration case [13] without cold rolling, compared to existing TTT diagrams for strain-free alloys [8–10].

- The pre-rolling grain size was changed to 20 μm corresponding to ASTM size 8 [27,59], and the cold rolling ratio was changed to $R = 0.3$. The updated values were used to calculate the nucleation site densities N_{0j} and the interface energy Γ_{disl} according to equations (17)–(19).

The model assumes one-way coupling between the temperature and the alloy microstructure. The thermal history at each node of the FE model was fed to the precipitation model to obtain the δ phase characteristics at each point of the sample. As was done for the calibration case, only the temperatures from the holding stage were taken into account during precipitation simulation. This assumption is expected to have little impact due to the high heating rates used in this study.

4. Results of FE/KWN coupling and discussion

The applicability of the proposed modeling approach is discussed in the following section by comparing the model hypotheses and predictions with the qualitative and quantitative results of the experimental case study obtained via SEM analysis.

4.1. SEM observations vs. KWN model hypotheses

The SEM-BSE images in Fig. 12 (a) and (b) show different zones along the longitudinal axis of the 920° C/1800 s sample. δ precipitates are present both inter- and intra-granularly. A general ellipsoidal shape can be observed for the precipitates. From the images taken in this study, no definitive link can be established between spatial distribution and aspect ratio. Nevertheless, one can note the presence of large, spheroidal δ precipitates along grain boundaries (yellow arrows), as well as thin needle-shaped δ arranged in straight lines − {1 1 1} planes − along dislocations (green chevrons). In particular, the grain boundary δ precipitates seem to appear exclusively on grain edges. Although by no means exact, this observation supports the choice to model grain edge precipitates as spheres and dislocation precipitates as needles.

In this study, an aspect ratio $q_{disl} = 7.6$ was chosen for the needle-shaped precipitates, assumed constant as a first
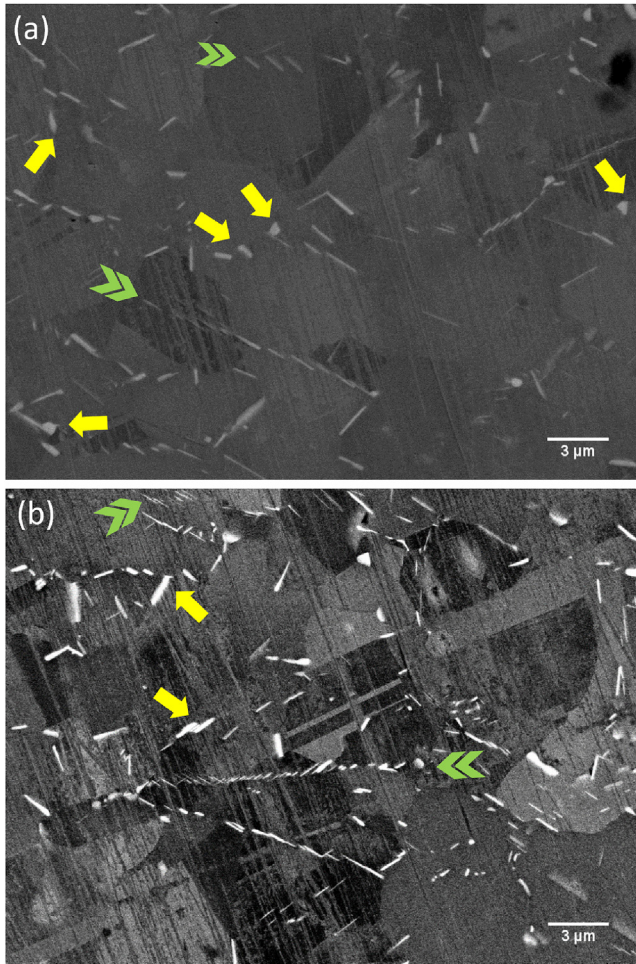
Fig. 12. SEM-BSE images of different zones on the 920° C/1800 s sample. (a) Central point, 920° C/1800 s (b) 15 mm from the central point, 880° C/1800 s. Yellow arrows indicate grain boundary δ phase, and green chevrons indicate δ phase along dislocations. (For interpretation of the references to colour in this figure legend, the reader is referred to the Web version of this article.)
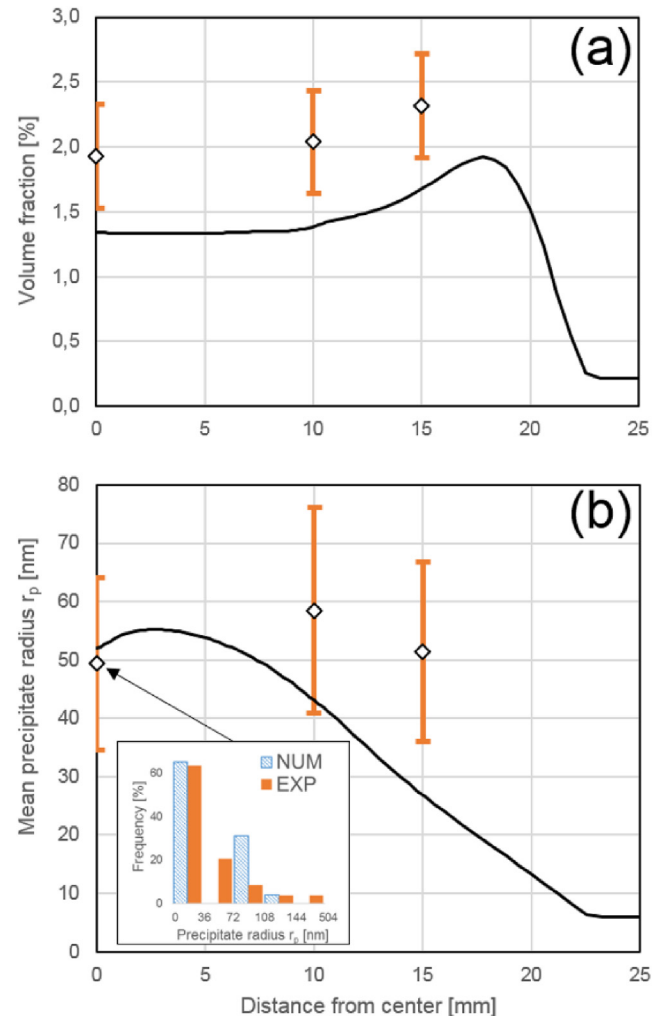

Fig. 13. Comparison of measured (points, EXP) and predicted (line, NUM) δ phase volume fraction (a) and mean radius r_p (b) along the longitudinal axis of the 920° C/ 1800 s sample. The size distribution at the central point is included in the bottom graph inset, with a bin size of 36 nm = 1 pixel.

approximation. 7.6 was the modal aspect ratio from the SEM analysis. Despite the large number of particles analyzed (above 3000 per measurement point) and the wide range of aspect ratios observed, the variation of this parameter with time and temperature [2] was not clearly reflected. Further quantitative investigations on the evolution of the precipitate morphology under different conditions, and with different cold rolling ratios [1], is of significant interest to complement efforts in modeling δ phase precipitation.

4.2. Predictions of the coupled FE-KWN model

Recall that the advantage of the proposed FE-KWN model is the ability to predict the evolution of delta phase characteristics at any point in the material without having to resort to heavy instrumentation. Fig. 13 shows the measured and predicted δ phase volume fraction and mean radius r_p[6] resulting from the heterogeneous heating along the longitudinal axis, predicted by the FE model in Fig. 6. The error bars indicate the uncertainty arising from the choice of grey level threshold and SEM resolution, as well as the

anisotropy about the measurement point. The closeness of the two results (numerical and experimental) is remarkable, especially given that no calibration has been performed on the evolution of the mean precipitate radius.

One sees that the measured δ phase fraction follows the same trend as the model predictions, but with an upwards shift of approximately 0.7 vol%. One possible explanation is the difference in heating rates between the calibration case [13] (furnace heating) and the present work (Joule heating), which may have an impact on recovery or recrystallization, as yet unaccounted for in the KWN model. Another possible reason for the overestimation is the assumption that surface fractions are equal to volume fractions, which holds if only superficial particles were observed. However, this is not strictly speaking valid in BSE mode, as the penetration of electrons into the sample surface reveals subsurface particles (in a layer estimated to be 150 nm thick, of the same order as the precipitate size).

With the chosen image processing parameters, long particles with a minor axis length of 1 pixel (about 30 nm) were included in the particle analysis. The precipitate radius r_p is considered to be the minor axis half-length of an ellipse fitted to the particle, leading to a minimum value of r_p close to half the pixel size or 15 nm. This gives confidence in the mean radii obtained from the SEM images.
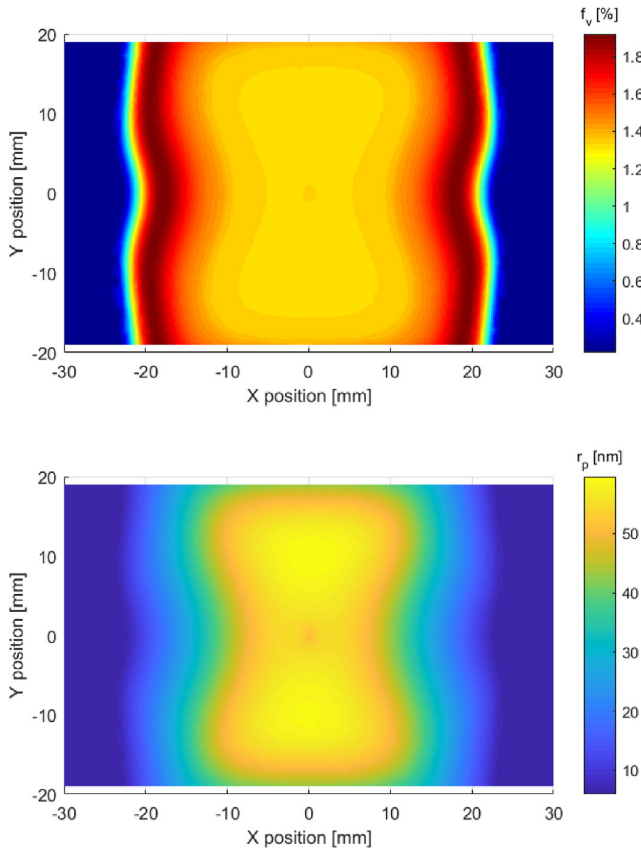
---

[6] During SEM analysis, r_p is taken to be the minor axis half-length of an ellipse fitted to the particle, in accordance with Fig. 7.

Fig. 14. δ phase volume fraction (top) and mean precipitate radius (bottom) topographies obtained for the 920° C heat-treated sample via the proposed approach.

In keeping with the observations made on Fig. 9, the current calibration of the KWN model does not account for the effect of the γ" phase below its solvus ($\sim$900° C). The addition of a γ" precipitate model in a future work should improve the model predictions at such temperatures.

Topographies of δ phase fraction and mean radius on the heat-treated samples are shown on Fig. 14(a) and (b) respectively, examples of how the proposed modeling approach aids in the design of alloy 718 parts subjected to complex heat treatments.

It is worth re-emphasizing that the proposed FE-KWN model coupling can be applied to cold deformed and heat-treated alloy 718 parts of any geometry, as long as the thermal history and local cold rolling reduction can be known (via FE modeling, for example).

5. Conclusions and perspectives

In this paper, a novel approach combining FE and KWN modeling was experimentally validated with an innovative high-throughput technique based on a direct resistance heating setup (Gleeble 3500), designed to drastically cut down experimental time. The highly heterogeneous temperature field and its effect on δ phase precipitation were studied. The main features of the present approach are:

- The experimental set-up allows to explore a large temperature domain with only one or few experiment(s).
- FE simulations lead to an accurate description of the heterogeneous temperature field within the sample.
- A KWN model has been developed to account for heterogeneous precipitation (i) on dislocations, and (ii) on grain edges simultaneously.

- The model has been parametrized to agree quantitatively with results of the literature for various temperatures and cold rolling ratios.
- When fed with the temperature field from the FE model, the KWN model gives an accurate description of the δ phase characteristics (volume fraction and radius) at various locations within the sample.

The proposed approach can be easily adapted to the modeling of any part geometry even when submitted to complex heat processes, representing a significant step towards faster and more robust characterization of the δ phase in alloy 718.

Future work can be directed at the experimental and numerical challenges discussed in this paper. Quantitative investigations on the shape and aspect ratio of the δ phase would give precious data with which the proposed KWN model can be fine-tuned. The effect of heating rate on recrystallization and recovery is also an interesting point to be explored further. The modeling and validation of a γ" model in a future work will complete the δ model developed in this study. The proposed model as well as experimental technique can also be adapted to more complex precipitation processes, a widely studied example being hot forging in which the effects of precipitate breakage and grain deformation are preponderant.

Appendix A. Calculation of grain edge and dislocation densities with cold rolling

In this paper, simplified models were used to calculate the grain edge and dislocation densities for a given cold rolling reduction ratio, owing to a lack of published experimental data on this phenomenon.

The following hypotheses were used:

- The dislocation and grain edge densities were assumed to vary linearly with cold rolling over the range of reduction ratios investigated ($\leq$ 65%);
- The undeformed grains were modeled as cubes of uniform edge length d;
- During cold rolling, volume is conserved with no expansion observed in the direction perpendicular to the cold rolling axis.

For a cold rolling reduction ratio $R = -(\Delta z)/z$, the plastic strain tensor can be expressed as (A.1) according to classic hypotheses on rolling [60,61]:

$$\overline{\overline{\varepsilon}}^{pl} = \begin{bmatrix} -\ln(1-R) & 0 & 0 \\ & 0 & 0 \\ : & & \ln(1-R) \end{bmatrix}_{(l,t,z)} \quad (A.1)$$

The (l, t, z) coordinates are shown in Figure A.15(a), with l being the cold rolling axis. As the plastic strain tensor is already deviatoric, the equivalent plastic strain is simply written as (A.2):

$$\varepsilon_{pl}^{eq} = \sqrt{\frac{2}{3}\overline{\overline{\varepsilon}}_{pl} : \overline{\overline{\varepsilon}}_{pl}} = -\frac{2}{\sqrt{3}}\ln(1-R) \quad (A.2)$$
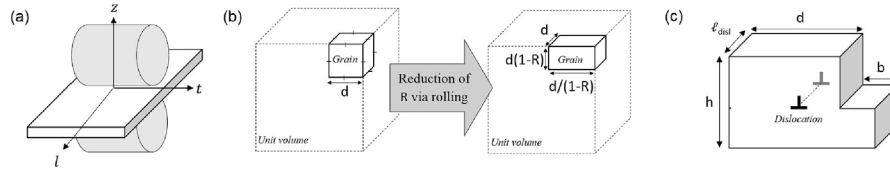
Fig. A.15. Schema for the calculation of nucleation site density. (a) Coordinate system of the cold-rolled sheet. Schematics used to calculate the evolution in (b) grain edge and (c) dislocation densities with cold rolling.

It follows that the plastic deformation of the grains, approximated here as cubes, is similar to that undergone by the sheet metal. From Figure A.15(b), the relation between grain edge density ρ_{edge} and R can be deduced as (A.3):

$$\rho_{edge} = n_{grain} L_{edge} = \frac{1}{d^2} \left(3 + \frac{R^2}{1-R} \right) \tag{A.3}$$

Where n_{grain} is the number of grains per unit volume, L_{edge} is the edge length of each grain, and d is the initial grain size.

Orowan's model was used to calculate the dislocation density for a given reduction ratio. Consider an elementary grain slice of thickness h containing a single dislocation as shown in Figure A.15(c). As the Burgers vector $b \ll d$, the dislocation density can be expressed as A.4:

$$\rho_{disl} = \rho_{disl}^0 + \frac{\ell_{disl}}{v_{elem}} = \rho_{disl}^0 + \frac{1}{dh} \tag{A.4}$$

where ρ_{disl}^0 is the initial dislocation density present in a recrystallized grain, ℓ_{disl} is the dislocation length within an elementary grain slice of volume v_{elem} (see figure A.15(c)).

As the grain distortion $\gamma = b/h$ should scale with the equivalent plastic strain calculated in (A.2), h can be replaced by (A.5):

$$h = \frac{b}{\gamma} \simeq \frac{b}{\varepsilon_{pl}^{eq}} \tag{A.5}$$

The dislocation density can now be related to the cold rolling reduction ratio via (A.6):

$$\rho_{disl} = \rho_{disl}^0 - \frac{2}{\sqrt{3}} \frac{\ln(1-R)}{bd} \tag{A.6}$$

References

[1] Y. Mei, Y. Liu, C. Liu, C. Li, L. Yu, Q. Guo, H. Li, Effects of cold rolling on the precipitation kinetics and the morphology evolution of intermediate phases in Inconel 718 alloy, J. Alloy. Comp. 649 (2015) 949—960.

[2] N. Vanderesse, M. Anderson, F. Bridier, P. Bocher, Inter- and intragranular delta phase quantitative characterization in Inconel 718 by means of image analysis, J. Microsc. 261 (2016) 79—87.

[3] S. Azadian, L.Y. Wei, R. Warren, Delta phase precipitation in inconel 718, Mater. Char. 53 (2004) 7—16.

[4] A.C. Yeh, K.W. Lu, C.M. Kuo, H.Y. Bor, C.N. Wei, Effect of serrated grain boundaries on the creep property of Inconel 718 superalloy, Mater. Sci. Eng. 530 (2011) 525—529.

[5] D.X. Wen, Y.C. Lin, Y. Zhou, A new dynamic recrystallization kinetics model for a Nb containing Ni-Fe-Cr-base superalloy considering influences of initial δ phase, Vacuum 141 (2017) 316—327.

[6] D. Cai, W. Zhang, P. Nie, W. Liu, M. Yao, Dissolution kinetics of δ phase and its influence on the notch sensitivity of Inconel 718, Mater. Char. 58 (2007) 220—225.

[7] P.P. Kañetas, L.R. Osorio, M.P.G. Mata, M.D.L. Garza, V.P. López, Influence of the delta phase in the microstructure of the inconel 718 subjected to delta-processing heat treatment and hot deformed, Procedia Materials Science 8 (2015) 1160—1165.

[8] W. Boesch, H. Canada, Precipitation reactions and stability of Ni3Cb in inconel alloy 718, in: Proceedings of the International Symposium on Structural Stability in Superalloys, 1968, pp. 579—596.

[9] A. Oradei-Basile, J. Radavich, A current t-t-t diagram for wrought alloy 718, Superalloys 718, 625 and Various Derivatives, 1991, pp. 325—335.

[10] V. Beaubois, J. Huez, S. Coste, O. Brucelle, J. Lacaze, Short term precipitation kinetics of delta phase in strain free Inconel* 718 alloy, Mater. Sci. Technol. 20 (2004) 1019—1026.

[11] G. Camus, Doctoral Thesis, >Traitements thermomécaniques de l'alliage NC 19 Fe Nb (Inconel 718) pour différentes applications sur turbomachines industrielles et aéronautiques, 1, INP, Toulouse, 1986, pp. 1—180.

[12] R. Decker, C. Sims, The Metallurgy of Nickel-base Superalloys, Paul D. Merica Research Laboratory, 1972.

[13] W. Liu, Z. Chen, M. Yao, Effect of cold rolling on the precipitation behavior of δ phase in INCONEL 718, Metall. Mater. Trans. 30 (1999) 31—40.

[14] A. Niang, B. Viguier, J. Lacaze, Some features of anisothermal solid-state transformations in alloy 718, Mater. Char. 61 (2010) 525—534.

[15] W. Wong-Ng, Evaluation of the current status of the combinatorial approach for the study of phase diagrams, J. Res. Natl. Inst. Stand. Technol. 117 (2012) 304.

[16] D. Campello, N. Tardif, M. Moula, M.C. Baietto, M. Coret, J. Desquines, Identification of the steady-state creep behavior of Zircaloy-4 claddings under simulated Loss-Of-Coolant Accident conditions based on a coupled experimental/numerical approach, Int. J. Solid Struct. 115—116 (2017) 190—199.

[17] E. Gumbmann, F. De Geuser, A. Deschamps, W. Lefebvre, F. Robaut, C. Sigli, A combinatorial approach for studying the effect of Mg concentration on precipitation in an Al-Cu-Li alloy, Scripta Mater. 110 (2016) 44—47.

[18] M. Avrami, Kinetics of phase change. II TransformationTime relations for random distribution of nuclei, J. Chem. Phys. 8 (1940) 212—224.

[19] R. Wagner, R. Kampmann, P.W. Voorhees, Homogeneous second-phase precipitation, in: Phase Transformations in Materials, January 2005, 2005, pp. 309—407.

[20] M. Perez, M. Dumont, D. Acevedo-Reyes, Implementation of classical nucleation and growth theories for precipitation, Acta Mater. 56 (2008) 2119—2132.

[21] M. Stockinger, E. Kozeschnik, B. Buchmayr, W. Horvath, Modelling of δ-phase dissolution during preheating of inconel 718 turbine disks, Superalloys 718, 625, 706 and Various Derivatives 1 (2001) 141—148.

[22] K. Wu, F. Zhang, S. Chen, W. Cao, Y. Chang, A modeling tool for the precipitation simulations of superalloys during heat treatments, Superalloys (2008) 933—939.

[23] R. Radis, G.A. Zickler, M. Stockinger, C. Sommitsch, E. Kozeschnik, Numerical simulation of the simultaneous precipitation of δ and γ' phases in the Ni-base superalloy ATI Allvac®718 Plus™, in: 7th International Symposium on Superalloy 718 and Derivatives 2010, vol. 2, 2010, pp. 569—578.

[24] H.Y. Zhang, S.H. Zhang, M. Cheng, Z.X. Li, Deformation characteristics of δ phase in the delta-processed Inconel 718 alloy, Mater. Char. 61 (2010) 49—53.

[25] D. Bardel, M. Perez, D. Nelias, A. Deschamps, C.R. Hutchinson, D. Maisonnette, T. Chaise, J. Garnier, F. Bourlier, Coupled precipitation and yield strength modelling for non-isothermal treatments of a 6061 aluminium alloy, Acta Mater. 62 (2014) 129—140.

[26] F. Perrard, A. Deschamps, P. Maugis, Modelling the precipitation of NbC on dislocations in α-Fe, Acta Mater. 55 (2007) 1255—1266.

[27] J. Deleume, J.-M. Cloué, E. Andrieu, Influence of δ phase precipitation on the stress corrosion cracking resistance of alloy 718 in PWR primary water, J. Nucl. Mater. 382 (2008) 70—75.

[28] C.A. Schneider, W.S. Rasband, K.W. Eliceiri, NIH Image to ImageJ: 25 years of image analysis, Nat. Methods 9 (2012) 671—675.

[29] J. Schindelin, I. Arganda-Carreras, E. Frise, V. Kaynig, M. Longair, T. Pietzsch, S. Preibisch, C. Rueden, S. Saalfeld, B. Schmid, J.-Y. Tinevez, D.J. White, V. Hartenstein, K. Eliceiri, P. Tomancak, A. Cardona, Fiji: an open-source platform for biological-image analysis, Nat. Methods 9 (2012) 676—682.

[30] L. Wojnar, K.J. Kurzydłowski, J. Szala, Quantitative image analysis, in: Metallography and Microstructures, Volume 9, ASM Handbook, ASM International, 2004, p. 1004.

[31] Dassault Systèmes Simulia Corp, Abaqus Analysis User's Guide, 2014.

[32] C. Zhang, M. Bellet, M. Bobadilla, H. Shen, B. Liu, Inverse finite element modelling and identification of constitutive parameters of UHS steel based on Gleeble tensile tests at high temperature, Inverse Probl. Sci. Eng. 19 (2011) 485—508.

[33] B.P. Keller, S.E. Nelson, K.L. Walton, T.K. Ghosh, R.V. Tompson, S.K. Loyalka, Total hemispherical emissivity of Inconel 718, Nucl. Eng. Des. 287 (2015) 11—18.

[34] J. Lienhard, A Heat Transfer Textbook, fourth ed., 2017.

[35] D. Chapman, High Conductivity Coppers for Electrical Engineering, 2016.
[36] Omega Engineering, Physical Properties of Thermoelement Materials, 2005.
[37] Special Metals Corporation, INCONEL alloy 718, 2007.
[38] Nickel Development Institute, High Temperature High Strength Nickel Base Alloys, 1995.
[39] United States Air Force 11, Military Handbook - Metallic Materials and Elements for Aerospace Vehicle Structures, 1998.
[40] J.A. Nelder, R. Mead, A simplex method for function minimization, Comput. J. 7 (1965) 308—313.
[41] Y. Desvallees, M. Bouzidi, F. Bois, N. Beaude, Delta phase in INCONEL 718: mechanical properties and forging process requirements, Superalloys 718, 625, 706 and Various Derivatives, 1994, pp. 281—291.
[42] M. Sundararaman, N. Sachin, B.S. Jung, V. Amit, P. Bhaskar, R. Kishore, Evolution of δ phase microstructure in alloy 718, in: 7th International Symposium on Superalloys 718 and Derivatives, 2010, pp. 737—750.
[43] M. Sundararaman, P. Mukhopadhyay, S. Banerjee, Precipitation of the δ-Ni3Nb phase in two nickel base superalloys, Metall. Trans. A 19 (1988) 453—465.
[44] R.P. Singh, J.M. Hyzak, T.E. Howson, R.R. Biederman, Recrystallization behavior of cold rolled alloy 718, Superalloys 718, 625 and Various Derivatives, 1991, pp. 205—215.
[45] M. Jouiad, E. Marin, R. Devarapalli, J. Cormier, F. Ravaux, C.L. Gall, J.-M. Franchet, Microstructure and mechanical properties evolutions of alloy 718 during isothermal and thermal cycling over-aging, Mater. Des. 102 (2016) 284—296.
[46] G. Lorimer, Precipitation at grain boundaries, J. Phys. Colloq. 36 (1975) 16.
[47] B. Holmedal, E. Osmundsen, Q. Du, Precipitation of non-spherical particles in aluminum alloys Part I: generalization of the kampmann-wagner numerical model, Metall. Mater. Trans. 47 (2016) 581—588.
[48] Q. Du, B. Holmedal, J. Friis, C.D. Marioara, Precipitation of non-spherical particles in aluminum alloys Part II: numerical simulation and experimental characterization during aging treatment of an Al-Mg-Si alloy, Metall. Mater. Trans. 47 (2016) 589—599.
[49] E. Kozeschnik, J. Svoboda, F. Fischer, Shape factors in modeling of precipitation, Mater. Sci. Eng. 441 (2006) 68—72.
[50] J. Russell, M. Lasonde, L. Jackman, Microstructure development and thermal response of delta processed billet and bar for alloy 718, Superalloys 718, 625, 706 and Various Derivatives, 2005, pp. 363—372.
[51] R.V. Patil, G.B. Kale, Chemical diffusion of niobium in nickel, J. Nucl. Mater. 230 (1996) 57—60.
[52] M. Karunaratne, R. Reed, Interdiffusion of niobium and molybdenum in nickel between 900 -1300 Â°C, Defect Diffusion Forum 237—240 (2005) 420—425.
[53] B. Ter-Ovanessian, C. Berrest, J. Deleume, J.-M. Cloué, E. Andrieu, Influence of interstitials content on the diffusion of Niobium in alloy 718, Defect Diffusion Forum 289—292 (2009) 161—166.
[54] A. Devaux, L. Nazé, R. Molins, A. Pineau, A. Organista, J.Y. Guédou, J.F. Uginet, P. Héritier, Gamma double prime precipitation kinetic in Alloy 718, Mater. Sci. Eng. 486 (2008) 117—122.
[55] Y.-f. Han, P. Deb, M.C. Chaturvedi, Coarsening behavior of y"- and y'-particles in Inconel alloy 718, Met. Sci. 16 (1982) 555—561.
[56] J. Blaizot, T. Chaise, D. Nélias, M. Perez, S. Cazottes, P. Chaudet, Constitutive model for nickel alloy 690 (Inconel 690) at various strain rates and temperatures, Int. J. Plast. 80 (2016) 139—153.
[57] P. Villars, Pearson's Handbook: Crystallographic Data for Intermetallic Phases, ASM International, Materials Park, OH, 1997.
[58] E. Kozeschnik, J. Svoboda, R. Radis, F. Fischer, Mean-field model for the growth and coarsening of stoichiometric precipitates at grain boundaries, Model. Simulat. Mater. Sci. Eng. 18 (2010).
[59] R.P. Guest, S. Tin, Modelling microstructural transformations of nickel base superalloy in 718 during hot deformation, Superalloys 718, 625, 706 and Derivatives, 2005, pp. 385—397.
[60] S. Schoenfeld, R. Asaro, Through thickness texture gradients in rolled polycrystalline alloys, Int. J. Mech. Sci. 38 (1996) 661—683.
[61] L. Delannay, J. Tacq, D. Bardel, M. Seefeldt, Direct micro-to-macro modelling of the cold rolling of pearlitic steel, in: MATEC Web of Conferences, volume vol. 80, p. 02008.